

Interface instabilities in hafnium hydride entrained iron metal matrix composites

M. Dunkin, A. Pattammattel

To be published in "Journal of Applied Physics"

February 2025

Photon Sciences

Brookhaven National Laboratory

U.S. Department of Energy

USDOE Office of Science (SC), Basic Energy Sciences (BES). Scientific User Facilities (SUF)










Notice: This manuscript has been authored by employees of Brookhaven Science Associates, LLC under Contract No. DE-SC0012704 with the U.S. Department of Energy. The publisher by accepting the manuscript for publication acknowledges that the United States Government retains a non-exclusive, paid-up, irrevocable, world-wide license to publish or reproduce the published form of this manuscript, or allow others to do so, for United States Government purposes.

DISCLAIMER

This report was prepared as an account of work sponsored by an agency of the United States Government. Neither the United States Government nor any agency thereof, nor any of their employees, nor any of their contractors, subcontractors, or their employees, makes any warranty, express or implied, or assumes any legal liability or responsibility for the accuracy, completeness, or any third party's use or the results of such use of any information, apparatus, product, or process disclosed, or represents that its use would not infringe privately owned rights. Reference herein to any specific commercial product, process, or service by trade name, trademark, manufacturer, or otherwise, does not necessarily constitute or imply its endorsement, recommendation, or favoring by the United States Government or any agency thereof or its contractors or subcontractors. The views and opinions of authors expressed herein do not necessarily state or reflect those of the United States Government or any agency thereof.

RESEARCH ARTICLE | JANUARY 02 2025

Interface instabilities in hafnium hydride entrained iron metal matrix composites

Mikaela R. Dunkin ; Mirza A. Shawon ; Mingxi Ouyang ; Jonathan M. Gentile ; Ajith Pattammattel ; Jason R. Trelewicz ; Lance L. Snead ; David J. Sprouster  



J. Appl. Phys. 137, 015105 (2025)

<https://doi.org/10.1063/5.0234481>



View Online



Export Citation

Articles You May Be Interested In

TbCu₇-type Sm-X-Fe compounds (X = Zr, Hf, Y, Dy, La, Ce and Nd) synthesized by low-temperature reduction-diffusion (LTRD) process using molten salt

AIP Advances (March 2022)

Mechanism of amorphous state formation, crystalline structure, and hyperfine interactions in DyMn_{6-x}Ge₆Fe_x ($0 \leq x \leq 6$) alloys

J. Appl. Phys. (October 2010)

Oxide or carbide nanoparticles synthesized by laser ablation of a bulk Hf target in liquids and their structural, optical, and dielectric properties

J. Appl. Phys. (May 2016)



Journal of Applied Physics

Special Topics Open for Submissions

[Learn More](#)









Interface instabilities in hafnium hydride entrained iron metal matrix composites

Cite as: J. Appl. Phys. 137, 015105 (2025); doi: 10.1063/5.0234481

Submitted: 21 August 2024 · Accepted: 12 December 2024 ·

Published Online: 2 January 2025



Mikaela R. Dunkin,¹  Mirza A. Shawon,¹  Mingxi Ouyang,¹  Jonathan M. Gentile,¹  Ajith Pattammattel,² 
Jason R. Trelewicz,^{1,3,4}  Lance L. Snead,¹  and David J. Sprouster^{1,a)} 

AFFILIATIONS

¹Department of Materials Science and Chemical Engineering, Stony Brook University, Stony Brook, New York 11794, USA

²National Synchrotron Light Source II, Brookhaven National Laboratory, Upton, New York 11793, USA

³Institute for Advanced Computational Science, Stony Brook University, Stony Brook, New York 11794, USA

⁴Materials Science and Technology Division, Oak Ridge National Laboratory, Oak Ridge, Tennessee 37831, USA

^{a)}Author to whom correspondence should be addressed: david.sprouster@stonybrook.edu

ABSTRACT

The chemical interactions in Fe–HfH₂ metal matrix composites (MMCs) are studied across multiple length scales to elucidate the decomposition of the parent phases and corresponding reaction zone physics during direct current sintering. Fe–HfH₂ composites were synthesized with increasing as-mixed hydride contents of Fe–25% HfH₂, Fe–40% HfH₂, Fe–55% HfH₂, and Fe–70% HfH₂ (all in vol. %) to demonstrate the ability to achieve sintered MMCs with target hydride contents. Samples were probed across multiple length scales through a multi-modal workflow employing x-ray diffraction, scanning electron microscopy and segmentation analysis, and synchrotron techniques including hard x-ray fluorescence mapping and nanoprobe x-ray absorption near-edge structure measurements. Under the selected sintering temperature and pressure conditions, hydrogen evolution is seen to evolve through parallel paths: thermal decomposition from during the transformation of HfH₂ to HfH_{x<2} and through subsequent reaction with the Fe matrix leading to intermetallic phase formation. Specifically, HfFe and HfFe₂ intermetallic formation accelerates the release of hydrogen with a subsequent HfO₂ phase forming at grain boundaries. For this MMC, the consumption or loss of hydrogen can be considerable in compacts with initial hydride loading of 25%–40% HfH₂ approaching 83% hydrogen loss for the lower volume fraction composites. Increasing the volume fraction of HfH₂ to 70% enhanced the retained hydrogen content to 53% and attributed to the reduced interfacial area intrinsic to the increased HfH₂ loading in this MMC.

© 2025 Author(s). All article content, except where otherwise noted, is licensed under a Creative Commons Attribution (CC BY) license (<https://creativecommons.org/licenses/by/4.0/>). <https://doi.org/10.1063/5.0234481>

I. INTRODUCTION

The rapid advancements in High Temperature Superconductors (HTSs) are leading several commercial entities to develop fusion power systems utilizing high-field HTS magnets.^{1–3} These HTS magnets facilitate the design of highly compact tokamak reactors, which present several advantages, including reduced plant costs, improved plasma control, and decreased electricity expenses.⁴ However, advanced shielding materials for these systems must overcome several challenges, including high neutron flux, extreme thermal conditions, and electromagnetic interference. Present day tokamaks use combinations of high-atomic-number, low-atomic-number, and neutron absorbing materials such as W, H₂O, and B.⁵ H₂O is effectively ruled out in compact fusion power

designs due to its limited temperature stability and its high susceptibility to neutron activation.⁶ Tungsten (W) and its alloys are being recognized as promising candidates for plasma-facing materials in fusion reactors owing to their high-temperature strength, superior thermal conductivity, and minimal sputtering rates.^{7–10} Despite its significant benefits, W exhibits notable disadvantages, including vulnerability to surface damage induced by plasma, degradation due to neutron irradiation, increased brittleness at ambient temperatures, and complex processing requirements.^{11–14} Boron and boron-compounds contain attractive neutron absorbing properties but suffer from instability under irradiation and burnout due to n- α reactions,¹⁵ making them ineffective long-term shielding solutions. Overcoming constraints in size, temperature, and material durability necessitates a transformative design approach to enable

17 January 2025 14:13:37

effective neutron management within compact, high-stress environments.

Recent interest in metal hydrides arises from their potential use as moderators, or reflectors, in high-temperature nuclear reactors. Some metal hydrides and alloys exhibit high-temperature strength, stability, good hydrogen retention, and ease of fabrication.¹⁶ Metal hydrides can store hydrogen atoms like liquid water, with the hydrogen nuclei effectively moderating fast neutrons and reducing neutron flux. Therefore, the effectiveness of neutron shielding is highly dependent on the hydrogen concentration.^{17,18} They also exhibit high thermal conductivity, electrical resistivity, hardness, and, in some cases, beneficial mechanical properties.¹⁶ A critical issue involves hydrogen transport under temperature gradients, which can cause neutronic instability due to thermal transport and irradiation-enhanced diffusion. This can lead to mechanical failure in the moderator, characterized by metal hydride embrittlement and significant volumetric expansion.¹⁹ One proposed solution involves the use of a radiation and structurally stable matrix to entrain a metal hydride phase, capable of high-performance neutron moderation and absorption. Essentially, these composites combine the benefits of low activation, radiation stable matrices with high neutron stopping performance of the entrained hydride phase,²⁰ in turn mitigating the risk associated with their radiation instability.

The ideal metal matrix for composite radiation shields should possess several key features, including ease of fabricability, relatively low cost, low hydrogen isotope permeability at expected operating temperatures, and good thermal conductivity. Additionally, moderate to high ductility and strength are advantageous. Iron and nickel are considered strong candidates for the radiation shield matrix owing to their low hydrogen isotope permeability, favorable fabrication characteristics, and excellent thermal conductivity. Compared to nickel, iron has significantly lower hydrogen isotope solubility, which is a critical factor for managing tritium inventory in fusion facilities. Specifically, the solubility of hydrogen isotopes in iron is approximately two orders of magnitude lower than in nickel.^{21,22} Moreover, at 500 °C, iron (3×10^{-11} mol H₂/m/s/Pa^{0.5}) exhibits about four times lower permeability to hydrogen isotopes than nickel (12×10^{-11} mol H₂/m/s/Pa^{0.5}).²³ Iron is also significantly more cost-effective and has slightly better thermal conductivity. Thus, considering cost, hydrogen isotope permeation, and hydrogen isotope solubility, iron emerges as a superior choice over nickel. To that end, our primary goal in materials selection is to identify a bulk material that is both structurally and neutronic stable. Consequently, a key criterion for choosing the matrix and entrained phase is that the resulting composite should adhere to the rule of mixtures and be easy to fabricate. Also, it should be capable of sintering to near-ideal density at relatively low temperatures to prevent dissociation of the hydride phase during the sintering process.

We have previously demonstrated a method to fabricate composites entrained with high volume fractions of ZrH₂ and other neutron moderating materials.^{24–27} While ZrH₂ is excellent at slowing neutrons down, this current work expands upon the previous neutron moderator concept seeking to incorporate highly neutron absorbing metal hydrides within an irradiation-stable matrix, creating simultaneously neutron moderating and absorbing

shield composites. A strong candidate moderating and absorbing material, hafnium hydride (HfH₂), having a moderate cross section for thermal neutron capture of 113 b/atom (where b-barns are the commonly accepted neutron cross section unit of 10⁻²⁴ cm) and a hydrogen number density near that of water, is chosen as entrainment into our iron-based metal matrix composites (MMCs). Future implementation of this composite hinges on understanding the underlying Fe–Hf–H interactions with this initial work focusing on the pristine microstructure.

Historically, the Hf–H system²⁸ has been extensively studied to determine its phases^{29–33} and physiochemical properties.^{34–37} The Hf–H phase diagram has several established phases. Hf metal has two stable allotropes, α -Hf (P6₃/mmc, hcp) and β -Hf (I4/mmm, fcc).³⁸ With H insertion, α -Hf forms a tetragonal phase (also known as a deformed cubic delta phase) in the range of $1.48 < x < 1.60$ δ' -HfH_x, $1.60 < x < 1.72$ δ -HfH_x, and finally a tetragonal phase $1.82 < x < 2.02$ ϵ -HfH_x, with precise atomic ratios still under debate.^{29–32,35} In 2023, Dottor defined a new phase, γ -HfH_x with a PtS phase structure, and solved the δ' -HfH_x structure³¹ utilizing neutron diffraction. Typical transition metal hydrides (MH₂) exhibit CaF₂ structures with the face-centered cubic (fcc) metal atom sublattice and H atoms occupying tetrahedral lattice sites. Group IVB transition metals also exhibit a face-centered tetragonal (fct) metal sublattice, also viewed as a body center tetragonal (bct) metal sublattice. Recent work has demonstrated that the structural instability of the cubic phases arises from splitting of bands at the Fermi level, driving the Jahn Teller effect, and has suggested Fermi surface instability as a useful description.³⁹ The electronic structure of HfH_{1.56} was also studied with photoelectron spectroscopy and synchrotron radiation in 1981.⁴⁰ Despite this history, there are still many research avenues open toward understanding the Hf–H system. Furthermore, there is little research into HfH₂ metal composites suggested here and their elemental interactions. This work seeks to elucidate the behaviors of Fe–HfH₂ MMCs with varying HfH₂ compositions across multiple length scales.

II. MATERIALS AND METHODS

A. Materials fabrication

Sample specimens were prepared via direct current sintering (DCS) as follows. Fe powder (Alfa Aesar, USA, 325 mesh, 98% purity) was mixed with 25, 40, 55, or 70 vol. % HfH₂ powder (Stanford Advanced Materials, USA, 200 mesh, 99% purity) via speed-mixing (FlackTek DAC-1100) at 800 rpm for 1 min. 20 g of each powder charge was loaded into a 25 mm-diameter graphite die inlaid with graphite foil and wrapped in carbon felt to reduce thermal losses. A thermocouple (K-type) inserted into the graphite die was utilized to monitor the temperature during sintering. Samples were sintered using a SinterLand LABOX-3010KF DCS system. Electrical contact was maintained during the displacement of the graphite die assembly by placing the sample under a 50 MPa static uniaxial compressive pressure. Each sample was heated at a rate of 100 °C/min and held at 1000 °C for 5 min prior to cooling at ambient temperatures. Vacuum pressure was set at 10 Pa throughout the sintering process to promote densification. After sintering, each sample was sandblasted to remove the graphite foil and potential contaminants. Prior to characterization, samples were

17 January 2025 14:13:37

mirror-polished to eliminate surface imperfections, roughness, and scratches using a standard set of SiC abrasive sheets and diamond suspension.

B. Materials characterization

Density was determined using the water displacement method based on Archimedes' principle.⁴¹ Relative density was determined via normalizing by the rule-of-mixture density, which accounted for the concentration of HfH₂ in each composite. X-ray diffraction patterns (XRD; Bruker D8 Advance) were collected to assess phase content and degree of hydrogen retention post-sintering. After phase identification, the lattice parameters, weight fractions, and grain sizes for each phase were allowed to be refined. Each XRD pattern was analyzed using Rietveld refinement⁴² with the TOPAS software (Bruker) with instrument-based broadening parameters fixed (fundamental parameters approach) and a four component polynomial background function. The crystallographic data from Dottor³¹ for the HfH₂ (I4/mmm) and δ'-HfH_{1.44} (Ibam) phases were included in refinements with atom positions and atomic displacement parameters fixed. The Fe-Hf intermetallic phases HfFe₂ (α-HfFe₂ Fd-3m), HfFe₂ (λ-P6₃/mmc), and HfO₂ (P21/c) were included with atomic positions and displacement parameters fixed using values reported within the literature.⁴³⁻⁴⁵ A minimum of 21 and maximum of 28 parameters were refined for each XRD pattern, depending on the number of phases, with minimal correlations between the grain size and weight fractions. Slightly higher correlations were observed between the lattice parameters for the HfO₂ phase and the background. The microstructure of each sample was examined using scanning electron microscopy (SEM; Tescan, Lyra 3) with an accelerating voltage of 10 kV in a backscattered electron (BSE) mode. BSE images were analyzed using Fiji image processing software⁴⁶ and the trainable Weka Segmentation⁴⁷ plugin package to determine the % area of each identifiable component. In short, this process involves hand selection of representative pixels and assigning each a "class" designation before running the available code to then classify the entire image. This process is iterative and allows correction for misassignment of pixel class through further selection and analysis. Three SEM images for each specimen (from different regions) were analyzed to determine mean areas and standard errors. The Fe-25% HfH₂ sample was further characterized at the Hard X-Ray Nanoprobe (HXN) beamline at the NSLS-II at Brookhaven National Laboratory (BNL). Two-dimensional scanning x-ray fluorescence (XRF) and spectroscopy measurements were collected to resolve the elemental⁴⁸ and chemical structure around nanometer-scale features of interest.^{49,50} A 10 × 10 × 0.1 μm³ sample lamella was prepared via focused ion beam (FIB) lift-out techniques in a FEI Helios Nanolab 600 dual-beam focused ion beam/scanning electron microscope (FIB/SEM) located at the Center for Functional Nanomaterials (CFNs) at BNL. A nominally 1 μm-thick cross-sectional lamella was removed from the bulk sample, welded to a copper Omniprobe lift-out grid, and subsequently thinned to approximately 100 nm for analysis. Incident x rays with a wavelength of 1.3051 Å and an energy of 9.5 keV were focused via Fresnel zoneplate nanofocusing optics to a ~30 × 30 nm² spot size. Two-dimensional XRF maps were collected employing scanning

times of 50 ms. Two-dimensional XRF spectral maps were processed and visualized in PyXRF⁵¹ and MIDAS.⁵² Nanoscale x-ray absorption near-edge spectroscopy (nano-XANES) around the Hf L_{III}-edge (9561 eV) were collected to quantify the atomic structure of Hf atoms located within the XRF maps with 30 nm spatial resolution. Two separate locations were probed with nano-XANES. The graphical user interface JFEFF was utilized to run FEFF9, an implementation of real-space multiple-scattering theory, to calculate and model Hf based XANES data at the Hf L_{III}-edge.⁵³ To date, there are no reported x-ray absorption near-edge structure (XANES) measurements of any HfH_x or Fe-Hf phases. Of the Hf L_{III}-edge XANES data reported, the majority are of oxides⁵⁴⁻⁵⁷ and silicates.^{58,59}

III. RESULTS AND DISCUSSION

A. Sintering of Fe-HfH₂ composites

Iron-hafnium hydride entrained MMCs were produced with increasing volume percent of HfH₂: Fe-25% HfH₂, Fe-40% HfH₂, Fe-55% HfH₂, and Fe-70% HfH₂ via DCS. Figure 1 depicts the sintering characteristics of a representative Fe-HfH₂ powder. A positive displacement, i.e., in the direction of the applied compressive force, is observed in Fig. 1(a). At temperatures below 370 °C, samples undergo densification, concluding at 1000 °C, wherein the displacement curve exhibited a consistent and gradual increase in rate.

Measured vacuum pressure during the sintering cycle is shown in Fig. 1(b). An initial surge in vacuum pressure occurred at ca. 70 °C, consistent with the release of any remaining moisture or adsorbed gases within either the sample or the chamber. Notably, distinctive peaks in the vacuum pressure curve were evident at approximately 390, 435, and 890 °C, signifying the release of gaseous substances that alter the observed vacuum pressure.⁶⁰ Recent work by Dottor and colleagues developed a Hf-H phase diagram with *in situ* neutron diffraction indicates HfH_x begins to decompose and form H₂ gas between 170 and 300 °C.³¹ Above this temperature, HfH_x phases are still present. Furthermore, above 800 °C, Hf metal forms and significant amounts of H₂ are expected to be lost. These values are supported in other thermal analyses of the Hf-H system.^{61,62} Additionally, the small amount of iron oxides present on the surface of the feedstock Fe powder release additional O₂ at 775 and 925 °C.^{63,64} The change in vacuum pressure around 890 °C potentially marks the formation of the intermetallic compound Fe-Hf. These findings align with reports in the scientific literature,⁶⁵⁻⁶⁷ which suggest that lower initial pressure during DCS results in higher density. Mechanisms governing densification of the Fe-HfH₂ MMCs are discussed below.

B. Microstructural analysis through SEM analysis

To understand the distribution of these phases within the microstructure and confirm the phase concentrations determined via XRD, SEM micrographs were collected for each sample in the BSE mode (Fig. 2). Contrast variation in BSE images arise from differences in Z (atomic number), and phase density with high-Z elements like Hf appear brighter while low-Z elements appear darker.⁶⁸ Similarly, denser phases appear lighter than their less

17 January 2025 14:13:37

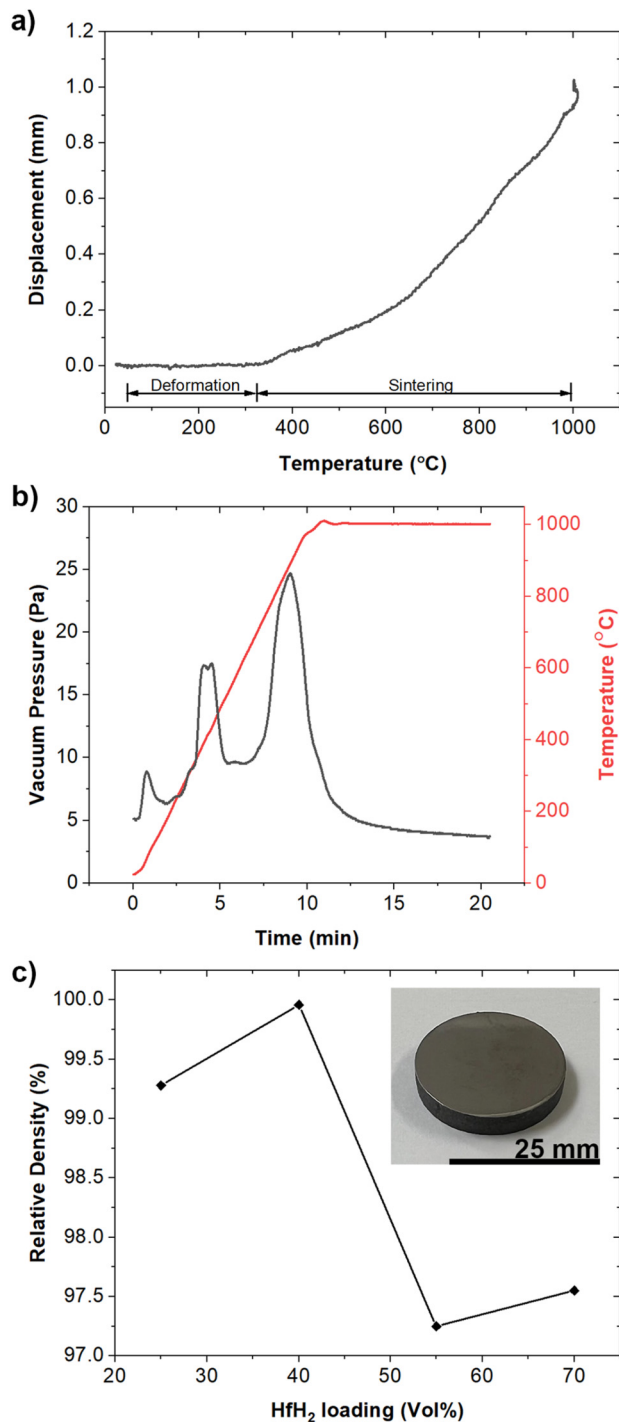


FIG. 1. For a representative Fe–25% HfH₂ sample, (a) the die displacement as a function of the sintering temperature and (b) the measured vacuum pressure during the sintering process, including sintering temperature. (c) The relative density of specimens sintered with varying vol. % of HfH₂, with an inset of a fully sintered 25 mm-diameter compact.

dense counterparts. In these images, the lightest areas are Hf-rich, containing HfH_x and HfO₂ phases, and the darkest areas are Fe-rich. Medium gray areas are the intermetallic phases, α -HfFe₂ and λ -HfFe₂. The authors note that the extremely dark regions viewable in the samples are from pullout areas arising from polishing and are not to be considered.

BSE images were further analyzed to quantify each area/phase present in the BSE images. Results from the SEM analysis (Table I) are compared with XRD phase refinement results and independently confirm the phase fraction percent determined by XRD. The Hf-rich phase percent for 55% and 70% samples increasingly diverge from that predicted by XRD due to these “pullout” zones. Qualitative analysis of the micrographs clearly indicates a growing area of the white, Hf-rich zones, consistent with the amount of HfH_x phases present. The light gray area, which consists of intermetallic phases, frequently separates the light, Hf-rich hydride, and oxide zone from the much darker, Fe-rich areas. Considering the starting materials, HfH₂ and Fe powder, the intermediate (in-between) intermetallic zone clearly forms as the starting materials interact and the free Hf and Fe atoms combine into intermetallic phases.

C. Phase determination with XRD

The behavior of the Fe–Hf–H interactions post-sintering was probed with XRD (Fig. 3 and Table I). Phase identification revealed each sample consists of body-centered cubic (BCC) Fe metal, Fe–Hf intermetallic phases (α -HfFe₂ and λ -HfFe₂), HfO₂, and multiple hafnium hydrides (HfH_{1.99} and δ' -HfH_{1.44}). Subtle differences in the weight fractions were determined when comparing between the SEM and XRD analysis due to the different inherent sensitivities and limitations of the two methods. SEM is poor at separating materials with similar Z-contrast (such as HfH_x phases and intermetallic phases), while XRD phase quantification can be complicated by overlapping diffraction peaks and weak scattering due to low-Z elements. The weight fractions and uncertainties reported in Table II for the Rietveld refinement are those directly from the non-linear least squares fitting method. The true uncertainty for the XRD weight fraction quantification is ~1%–2%.⁶⁹ Table II lists the weight fractions determined from both the XRD and SEM analysis with the realistic weight uncertainties. It is interesting to note that the quantification from the XRD and SEM for the 40% and 55% HfH₂ samples agrees within uncertainty ranges, while the extremes (25% and 70%) show discrepancies. These discrepancies result from a variety of factors, namely, the different length scale probed by each technique, and similar Z-contrast limiting isolation of Hf-rich intermetallic and oxide phases. Furthermore, these samples were prone to “pullout” during polishing leading to more dark regions on the sample surface. These dark/black areas were best resolved in the 25% sample and became increasingly difficult to differentiate from the dark, Fe-rich areas in the 70% sample. The differences in the weight fractions from XRD and SEM for the low Fe-rich and Hf-rich are the source of this discrepancy. Additionally, the thin nature of the HfO₂ phase (as discussed in Sec. III D) potentially hinders the correct incorporation into the Hf-rich phase analysis.

Of note, the δ' -HfH_{1.44} phase was recognized as the recently identified δ' -HfH_{1.44} structure determined by Dottor in 2023.³¹

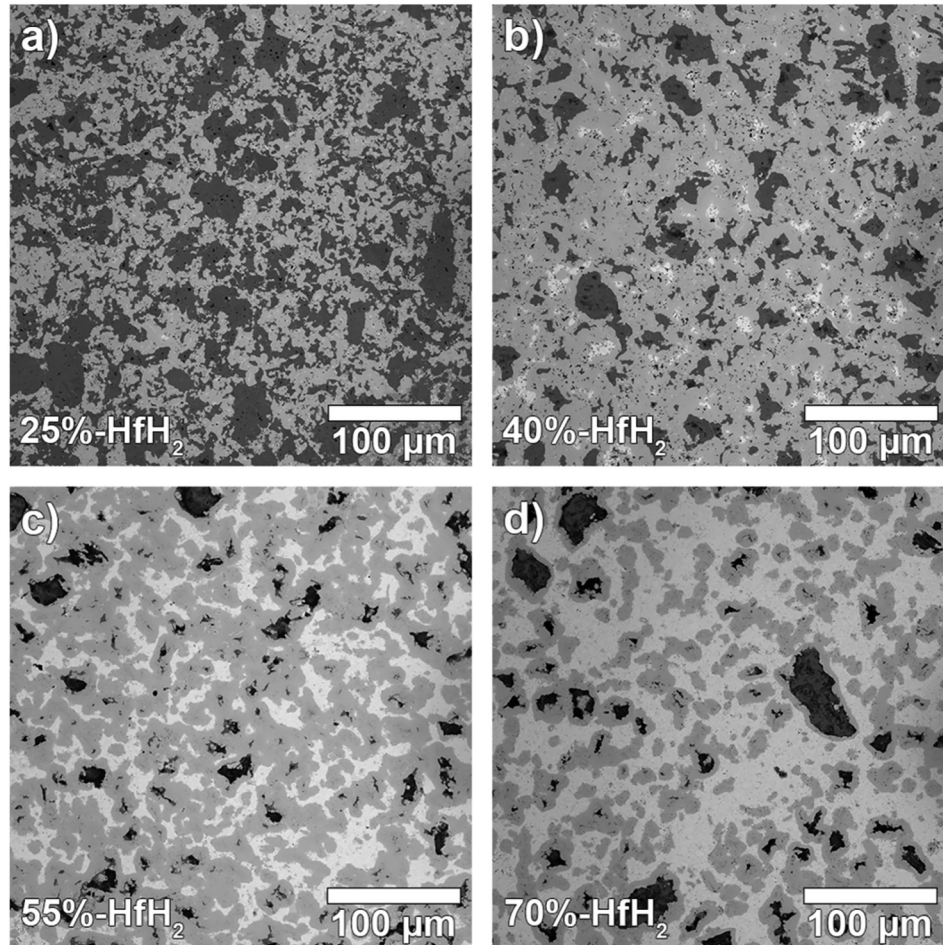


FIG. 2. Representative scanning electron microscopy (SEM) micrographs collected in the backscattered secondary electron (BSE) mode of (a) Fe-25% HfH₂, (b) Fe-40% HfH₂, (c) Fe-55% HfH₂, and (d) Fe-70% HfH₂.

Overall, sintering of HfH₂ with Fe powder induces changes to the hydride structure, forming additional phases which have been extensively documented in phase diagrams^{28,70,71} and through XRD studies.^{29,32,35} Unfortunately, few works have examined the Hf-H system at temperatures >800 °C, with only a single work noting the system is undefined at 1000 °C and 1 atm H₂.²⁸ The concomitant formation of lower ratio hydride phases along with HfO₂ and Hf-Fe intermetallic phases suggests that the sintering process results in a net loss of detectable hydrogen phases. Dehydrogenation has been noted before in TiH₂ analogs, starting at the particle or compact surface and progressing inward to the interior, creating a hydrogen concentration gradient.⁷² A uniform distribution of hydrogen (and hydride) concentration over the hafnium-sample volume is impeded by low mobility of hydrogen in the hafnium hydride and its weak solubility in the metal lattice.³⁴ Low hydrogen mobility in the Hf-H system has been attributed to vacancy sizing effects necessitating H be first reduced to become mobile.²⁹ Finally, dissolved oxygen in the Hf lattice tends to decrease H solubility,⁷³

TABLE I. Results of Weka Segmentation on SEM-BSE micrographs. Standard deviations from the SEM analysis are given in brackets ().

Sample	Phase	SEM % (standard deviation)	XRD
Fe-25% HfH ₂	Fe-rich	41.6 (1.2)	48.8 (2.0)
	Intermetallic	53.3 (1.1)	46.2 (2.0)
	Hf-rich	5.1 (1.0)	10.6 (2.0)
Fe-40% HfH ₂	Fe-rich	21.2 (1.5)	21.4 (2.0)
	Intermetallic	69.5 (2.3)	68.0 (2.0)
	Hf-rich	9.3 (0.5)	10.5 (2.0)
Fe-55% HfH ₂	Fe-rich	6.0 (0.9)	4.7 (2.0)
	Intermetallic	68.7 (2.9)	63.4 (2.0)
	Hf-rich	25.7 (1.4)	31.9 (2.0)
Fe-70% HfH ₂	Fe-rich	7.1 (1.5)	2.0 (2.0)
	Intermetallic	46.9 (1.0)	41.3 (2.0)
	Hf-rich	46.0 (1.3)	56.8 (2.0)

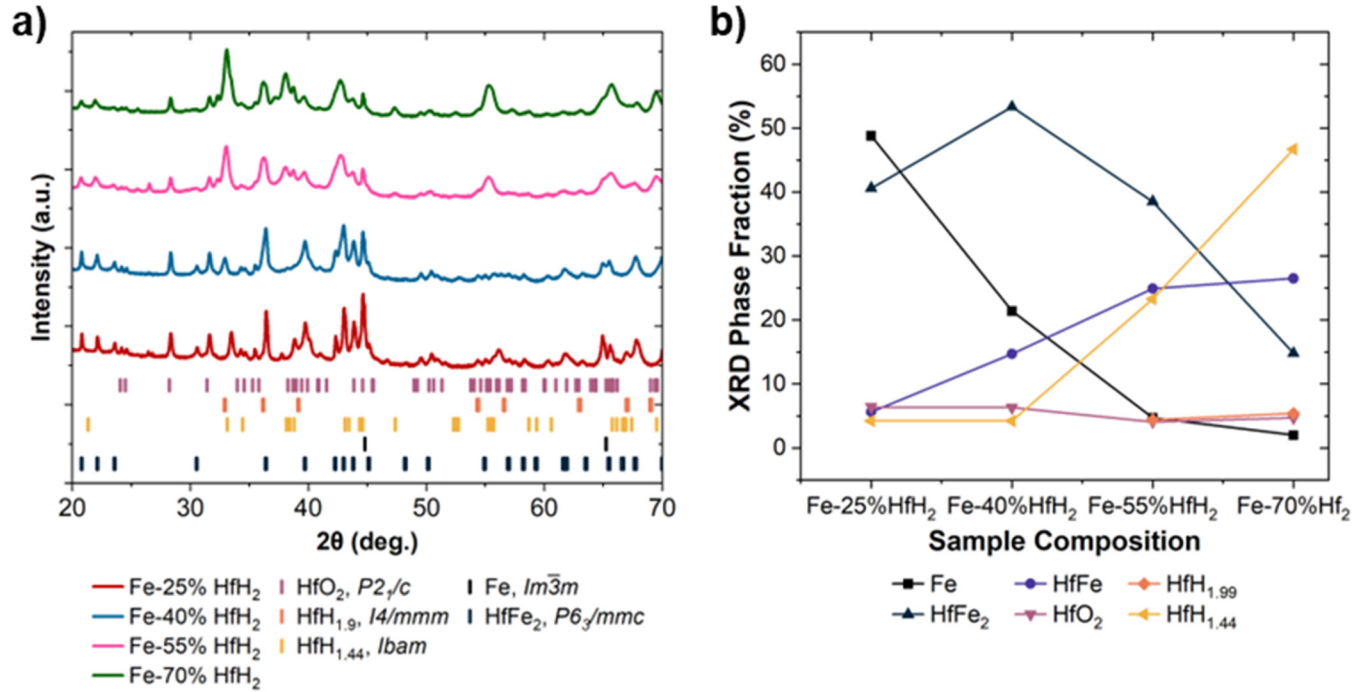


FIG. 3. (a) XRD results of the Fe-*n*% HfH₂ series where *n* = 25, 40, 55, and 70 and (b) XRD phase fraction vs sample composition.

TABLE II. Results of Rietveld refinement. Uncertainties from the non-linear least squares fitting method are given in parenthesis.

Sample	Phase name	Space group	a (Å)	b (Å)	c (Å)	beta (°)	Weight fraction (%) (error)	
			Value (error)	Value (error)	Value (error)	Value (error)		
Fe-25% HfH ₂	Fe	Im-3m	2.868 86 (1)	48.8(2)	
	α-HfFe ₂	Fd-3m	6.997 8 (3)	5.6(3)	
	λ-HfFe ₂	P6 ₃ /mmc	4.928 42 (8)	...	8.024 1(2)	...	40.6(2)	
	HfO ₂	P21/c	5.119 8 (5)	5.171 7(5)	5.297 4(5)	99.169(7)	6.4(1)	
	HfH _{1.44}	Ibam	4.650 (1)	9.282(3)	4.627 2(9)	...	4.2(1)	
	Fe-40% HfH ₂	Fe	Im-3m	2.869 18 (5)	21.4(2)
Fe-40% HfH ₂	α-HfFe ₂	Fd-3m	6.995 8 (4)	14.7(3)	
	λ-HfFe ₂	P6 ₃ /mmc	4.934 5 (1)	...	8.031 6(3)	...	53.3(2)	
	HfO ₂	P21/c	5.118 9 (6)	5.177 5(7)	5.293 3(6)	99.15(1)	6.3(1)	
	HfH _{1.44}	Ibam	4.712 (2)	9.418(4)	4.610(2)	...	4.2(9)	
	Fe-55% HfH ₂	Fe	Im-3m	2.869 6 (1)	4.7(1)
	α-HfFe ₂	Fd-3m	7.026 2 (3)	24.9(3)	
Fe-55% HfH ₂	λ-HfFe ₂	P6 ₃ /mmc	4.946 5 (3)	...	8.055 3(8)	...	38.5(3)	
	HfO ₂	P21/c	5.130 (1)	5.185(1)	5.282(1)	99.11(1)	4.1(1)	
	HfH _{1.9}	I4/mmm	3.375 (8)	...	4.78(2)	...	4.4(2)	
	HfH _{1.44}	Ibam	4.733 2 (4)	9.414 1(8)	4.646 8(2)	...	23.3(1)	
	Fe-70% HfH ₂	Fe	Im-3m	2.868 8 (1)	2.0(1)
	α-HfFe ₂	Fd-3m	7.022 6 (4)	26.5(3)	
Fe-70% HfH ₂	λ-HfFe ₂	P6 ₃ /mmc	4.941 3 (8)	...	8.027(1)	...	14.8(3)	
	HfO ₂	P21/c	5.126 (1)	5.185(1)	5.285(1)	99.12(1)	4.7(1)	
	HfH _{1.9}	I4/mmm	3.222 7 (4)	...	4.830(1)	...	5.4(5)	
	HfH _{1.44}	Ibam	4.727 9 (1)	9.382 6(5)	4.691 4(2)	...	46.7(4)	

17 January 2025 14:13:37

further reducing mobility and increasing the likelihood H will migrate in alternative paths.

A comparison of the XRD phase fraction vs sample composition is provided in Fig. 3(b). The HfO_2 phase fraction remains constant across all four samples, suggesting the HfO_2 phase reaches a stable equilibrium concentration despite the starting composition. The authors note that some percentage of the HfO_2 formation is related to a surface phenomenon, with HfO_2 forming upon exposure to air. The δ' - $\text{HfH}_{1.44}$ phase shares an inverse relationship with the Fe metal phase fraction, suggesting that Hf readily reacts with Fe, preferentially forming the intermetallic phases. Additional free Hf and Fe atoms form intermetallic λ - HfFe_2 and α - HfFe_2 phases. Phase diagrams of the Hf-Fe system indicate HfFe_2 phases are stable at higher atomic percentages of available Hf, nominally 33%.⁷⁴ While this availability is slightly out of range for the 25% HfH_2 sample, this behavior would be observable at a local level. Interestingly, the λ - Hf_2Fe phase is highest in the 25% HfH_2 sample, with its presence decreasing as the initial amount of HfH_2 increases. At the same time, the α - HfFe_2 shows a steady increase

before both intermetallic phases reach $\sim 20\%$ phase fractions. There is, thus, a clear interplay between the intermetallic phases, with the Fe matrix incorporating additional Hf as more is readily available.

D. Hard x-ray nanoprobe

The 25% HfH_2 sample was selected for HXN analysis due to the low hydride content representing the extreme case scenario for this sample series. Further characterization was necessary to determine the physio-chemical structure around nanometer-scale features of interest observed through SEM-BSE mapping. 2D XRF mapping was collected of the 25% HfH_2 sample, as shown in Fig. 4. Examination of the 2D XRF map collected of the $10 \times 10 \times 0.1 \mu\text{m}^3$ sample lamella reveals the presence of two distinct regions: an Fe-rich matrix with Hf-rich particles embedded. Within the Hf-rich particles, there are smaller Fe-rich particulates. These results are consistent with the SEM-BSE images in Fig. 2(a). Within the XRF map of the 25% HfH_2 lamellae, two locations, as indicated by the colored boxes, were further analyzed using nano-XANES around the Hf L_{III} -edge. Spectroscopic analysis was performed on this imaging stack to resolve the local atomic structure of the different Hf environments with 30 nm spatial resolution. Both Hf-rich particles exhibit a mottled appearance, with a sizable portion of their bulk consisting of lower Hf concentrations.

Reference XANES spectra of relevant materials ($\text{HfH}_{1.99}$, HfO_2 , α - HfFe_2 , and λ - HfFe_2) were generated and are shown in Fig. 5. The Hf L_{III} -edge XANES of HfO_2 agrees well with the literature,^{54,56,57,75} with a strong white line attributed to transition of a 2p electron to the 5d unoccupied state and a post-edge signal arising from multiple-scattering events affected by Hf-O disorder. To the best of the authors' knowledge, there are no prior experimental works of the HfH_x or Hf-Fe intermetallic XANES

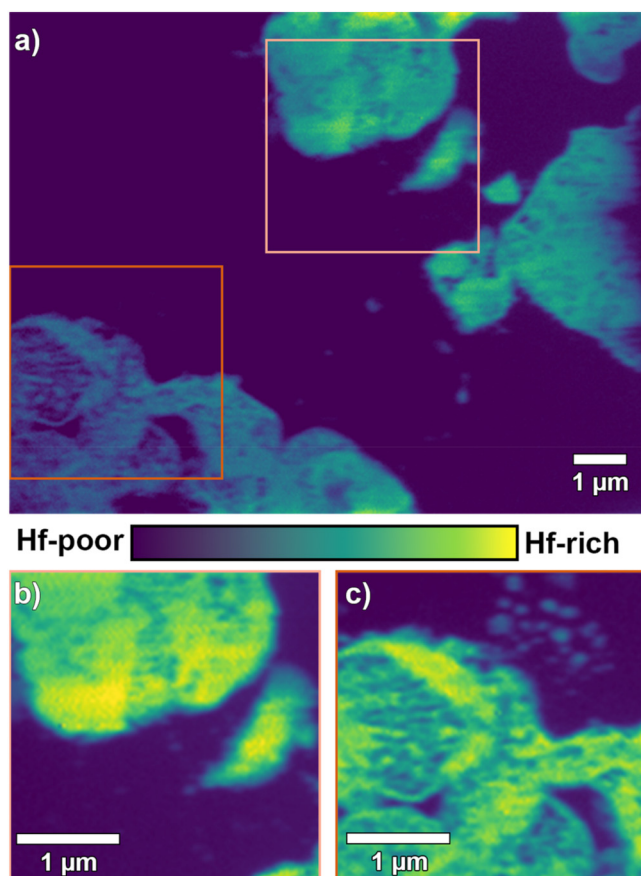


FIG. 4. X-ray fluorescence (XRF) maps collected of the Hf L_{III} -edge of a (a) Fe-25% HfH_2 lamellae. Colored boxes indicate two areas were further probed with nano-XANES at (b) location 1 and (c) location 2.

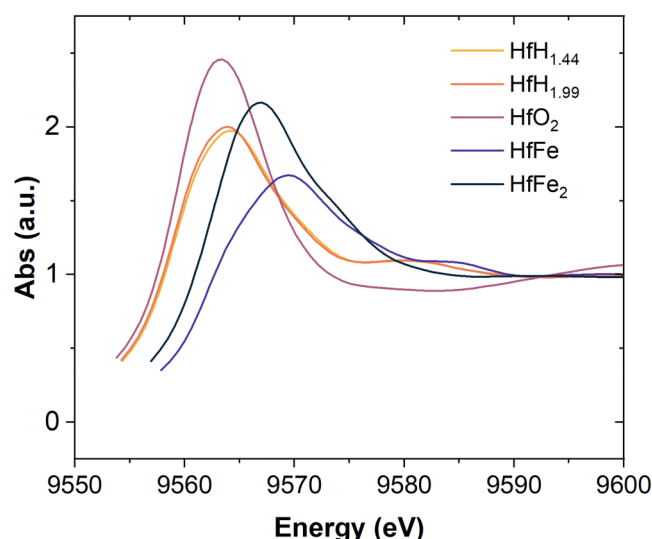


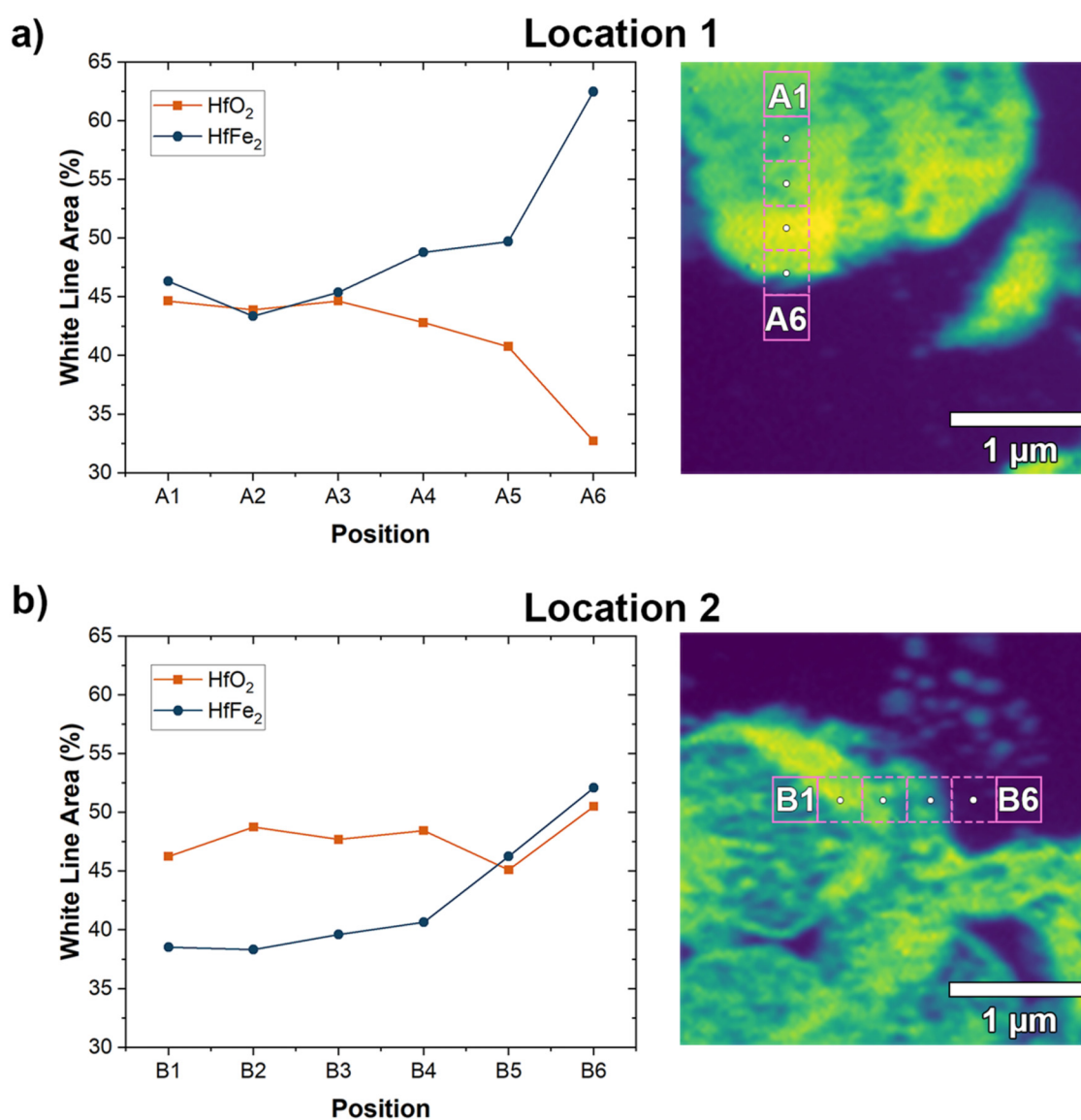
FIG. 5. FEFF generated Hf L_{III} -edge x-ray absorption near-edge structure (XANES) of relevant reference materials.

17 January 2025 14:13:37

structures. In the modeled spectra, the significant loss of white line intensity from the λ -HfFe₂ to the α -HfFe₂ indicates a filling of 5d orbitals. This behavior is also noted in the HfO₂, HfH_{1.99}, and δ' -HfH_{1.44} phase samples, with the O having additional available electrons to donate. Notably, the difference between the HfO₂ and HfH_{1.99} phases is <1 eV, making their structures difficult to resolve.

To probe phase differences across the Hf-rich particle, the Fe-rich/Hf-deficient matrix, and the boundary between them, regions of interest were selected at regular intervals in both location 1 and location 2 (Fig. 6). Fingerprinting analysis of the resultant

XANES spectra indicates the Hf-rich region consists of a mixture of HfO₂ and Hf-Fe intermetallic phases. This analysis was confirmed by fitting the white line peak with two pseudo-Voigt functions (1:1 Lorentzian: Gaussian relationship) centered at 9563.0 eV for HfO₂ and 9566.6 for HfFe₂. The similar peak centroid energies of 9563.0 and 9563.7 eV between HfO₂ and HfH_{1.99}, respectively, were a significant hurdle in resolving these structures. Given the open-air environment and the nanometer-thickness of the sample lamellae, it was concluded that HfO₂ would dominate the signal and, thus, a peak centroid of 9563.0 eV was selected to probe. The



17 January 2025 14:13:37

FIG. 6. Analysis of nano-XANES collected of the Hf L_{III}-edge at (a) location 1 and (b) location 2. Specific positions were probed linearly across each location from A1 to A6 for location 1 and B1 to B6 for location 2.

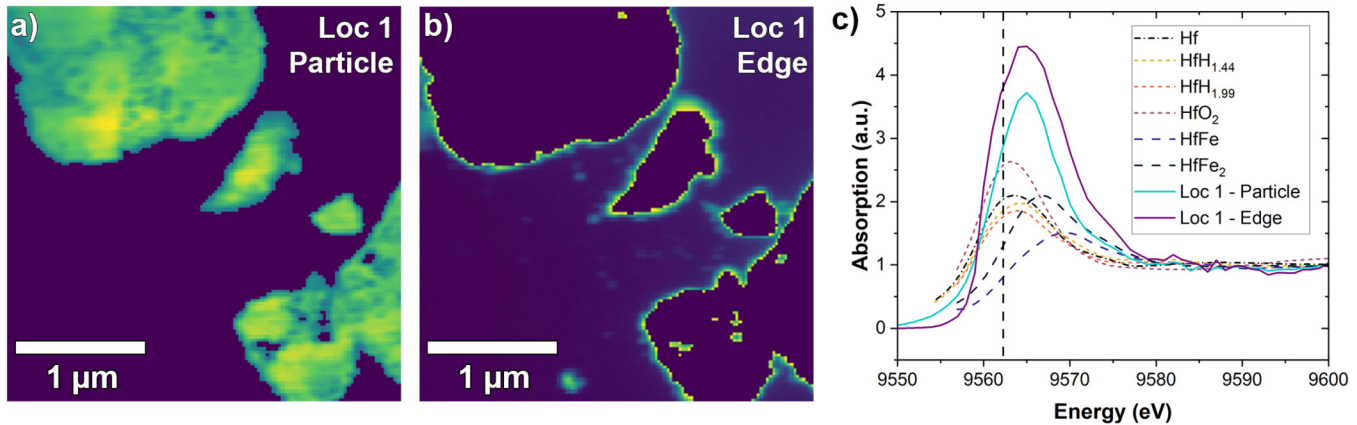


FIG. 7. Results of phase cluster analysis of nano-XANES of the Hf L_{III} -edge of the Fe-25% HfH_2 sample taken at location 1. Composite XRF maps of the (a) particle and (b) edge correlate with the XANES spectra in (c), where they are compared to the JFEFF-generated reference spectra.

authors note the presence of $HfH_{1.99}$ detected via XRD is minor (within the error of XRD phase quantification) (Fig. 3); and furthermore, its presence was difficult to confirm with XANES.

Moving from inside the Hf-rich particle toward the edge, there is a marked change in the white line intensity. Outside the Hf-rich particle, the white line is so intense it is indistinguishable from the background noise found throughout the sample. This is due to the low-negligible signal from Hf within the Fe-rich matrix. Notably, the signal near the edge of a particle indicates a reasonable increase in white line intensity, particularly in location 1. This nano-XANES area was probed with cluster analysis, available as a part of the MIDAS package.⁵² Analysis confirmed the line scan methodology and indicated two predominant regions: the particle core and the particle edge or “crust,” as shown in Figs. 7(a) and 7(b). Comparison of the resultant XANES with the JFEFF-generated reference materials in Fig. 7(c) confirms the Hf-rich particle core is a mixture of HfO_2/HfH_x with Hf-Fe intermetallic phases. Interestingly, the resulting cluster spectra for the edge have a distinct pre-edge shoulder feature, indicating a distinct phase not found within the particle. The energy of this feature most closely resembles the HfO_2 phase spectra.

Given the formation of Hf-Fe intermetallic phases, and the low remaining HfH_x phases post-sintering for the Fe-25% HfH_2 composite, it is reasonable to conclude that the area probed by the HXN experiments is the boundary between the Hf-Fe intermetallic phase and the Fe-rich matrix phase [with additional confirmation shown in the SEM-BSE and Fig. 2(a)]. The presence of the HfO_2 between these areas is a striking discovery. During processing, decomposition of the hydride phase is noted by its decreased presence from XRD patterns. Outside of the remaining hydride particles, H atoms unable to leave the structure become trapped along grain boundaries between the growing intermetallic phase and the consumed Fe and HfH_2 particles. As such, during cooling, the Hf at the surface recombines with any available O to form the HfO_2 phase, potentially accelerated by free H.

In the Fe- $n\%$ HfH_2 ($n = 25, 40, 55,$ and 70) MMCs, the HfH_2 undergoes limited decomposition during sintering, mitigated by the short times (5 min) at high temperature ($1000^\circ C$), while achieving full matrix density. Atomic hydrogen released from the HfH_x phases can potentially have a cleaning effect on the surface of surrounding Fe particles, increasing surface activity,⁷² and promoting interactions between the newly available Hf. The Fe and Hf will readily interact at these temperatures to form intermetallic phases.⁷⁶ It is interesting to note that at the higher HfH_2 loadings ($n = 40-70$), there is significant remaining HfH_x , presumably due to the short times at the high processing temperature, sluggish decomposition, and high surface areas of initial HfH_2 particles. This points to a potential pathway to engineer Fe-based composites with more hydrogen retention through interface control (i.e., pre-oxidizing HfH_2 particles). The XANES and XRF results in Fig. 7 highlight that the HfO_2 formation between the Fe and HfH_2 particles could be utilized to enable the former. Alternatively, directly incorporating larger format HfH_2 inclusions within the Fe host (wires or chopped fibers) where surface effects would be minimized/negligible could be explored.

IV. CONCLUSIONS

Iron-hafnium hydride entrained metal matrix composites were produced via sintering with varying HfH_2 loading including Fe-25% HfH_2 , Fe-40% HfH_2 , Fe-55% HfH_2 , and Fe-70% HfH_2 (all in vol. %). This work focuses on the Fe-Hf-H interactions at phase boundaries post-sintering across multiple length scales using XRD, SEM, XRF, and nano-XANES. XRD revealed each sample undergoes a varied degree of decomposition and reaches an equilibrium state of $HfH_{1.99}$ and HfO_2 , around 3.5 and 5% XRD phase fraction, respectively. A unique hydride phase, δ' - $HfH_{1.44}$, was identified in each sample. Likewise, the pure Fe metal phase decreases from initial concentration in each sample and decreases to a markedly lower percentage in the 55% and 70% HfH_2 samples. This work demonstrates that HfH_2 and Fe particles, under heat and

pressure during direct current sintering processing, form intermetallic phases, HfFe and HfFe₂. However, while decomposition and intermetallic formation are simultaneously occurring during processing, a significant fraction of hydrogen is retained HfH_{1.44} within the sintered MMC. The retained hydrogen content is a function of the original HfH₂ loading with a maximum value of 53% for the initial Fe-70% HfH₂ compact. Phase decomposition and subsequent chemical interactions at the interfaces between the entrained hydrides and metallic Fe matrix were mapped via SEM-BSE, which reveals the intermetallic phases form between Hf-rich and Fe-rich areas, and further confirmed by hard x-ray nanoprobe XRF and nano-XANES signaling the formation of HfO₂ at the boundary between the intermetallics and remaining Fe matrix.

ACKNOWLEDGMENTS

This work was supported by the Advanced Research Projects Agency-Energy (ARPA-E) Galvanizing Advances in Market-Aligned Fusion for an Overabundance of Watts (GAMOW) program under Contract No. DE-AR0001381. This research used resources at the hard x-ray nanoprobe beamline of the National Synchrotron Light Source II, a U.S. Department of Energy (DOE) Office of Science User Facility operated for the DOE Office of Science by Brookhaven National Laboratory under Contract No. DE-SC0012704. This research used the electron microscopy facility of Center for Functional Nanomaterials, which is a U.S. DOE Office of Science Facility, at Brookhaven National Laboratory also under Contract No. DE-SC0012704. We want to thank and acknowledge the two anonymous referees for their important and insightful comments that have helped strengthen this article.

AUTHOR DECLARATIONS

Conflict of Interest

The authors have no conflicts to disclose.

Author Contributions

Mikaela R. Dunkin: Conceptualization (equal); Data curation (equal); Formal analysis (equal); Investigation (equal); Methodology (equal); Validation (equal); Writing – original draft (equal). **Mirza A. Shawon:** Formal analysis (equal); Writing – original draft (supporting). **Mingxi Ouyang:** Formal analysis (equal). **Jonathan M. Gentile:** Investigation (supporting). **Ajith Pattammattel:** Investigation (supporting). **Jason R. Trelewicz:** Conceptualization (equal); Funding acquisition (equal); Investigation (equal); Methodology (equal); Project administration (equal); Resources (equal); Supervision (equal); Validation (equal); Writing – review & editing (equal). **Lance L. Snead:** Conceptualization (equal); Formal analysis (equal); Funding acquisition (equal); Investigation (equal); Methodology (equal); Project administration (equal); Resources (equal); Supervision (equal); Validation (equal); Writing – original draft (equal); Writing – review & editing (equal). **David J. Sprouster:** Conceptualization (equal); Data curation (equal); Formal analysis (equal); Funding acquisition (equal); Investigation (equal); Methodology (equal);

Project administration (equal); Resources (equal); Software (equal); Supervision (equal); Writing – original draft (equal); Writing – review & editing (equal).

DATA AVAILABILITY

The data that support the findings of this study are available from the corresponding author upon reasonable request.

REFERENCES

- ¹Y. Zhai, D. van der Laan, P. Connolly, and C. Kessel, “Conceptual design of HTS magnets for fusion nuclear science facility,” *Fusion Eng. Des.* **168**, 112611 (2021).
- ²L. Zimmerman, *Superconductor Technology for Smaller, Sooner Fusion* (MIT News, 2020).
- ³General Atomics and Tokamak Energy Join Forces on HTS Magnet Tech, *Nuclear Newswire* (American Nuclear Society, 2023). See <https://www.ans.org/news/article-5057/general-atomics-and-tokamak-energy-join-forces-on-hts-magnet-tech/>
- ⁴A. Sykes, M. P. Gryaznevich, D. Kingham, A. E. Costley, J. Hugill, G. Smith, P. Buxton, S. Ball, S. Chappell, and Z. Melhem, “Recent advances on the spherical tokamak route to fusion power,” *IEEE Trans. Plasma Sci.* **42**(3), 482–488 (2014).
- ⁵T. Hayashi, K. Tobita, S. Nishio, K. Ikeda, Y. Nakamori, and S. Orimo, “Neutronics assessment of advanced shield materials using metal hydride and borohydride for fusion reactors,” *Fusion Eng. Des.* **81**(8), 1285–1290 (2006).
- ⁶Y. Ikeda, Y. Uno, F. Maekawa, D. L. Smith, I. C. Gomes, R. C. Ward, and A. A. Filatenkov, “An investigation of the activation of water by D-T fusion neutrons and some implications for fusion reactor technology,” *Fusion Eng. Des.* **37**(1), 107–150 (1997).
- ⁷B. I. Khripunov, V. S. Koidan, A. I. Ryazanov, V. M. Gureev, S. N. Kornienko, S. T. Latushkin, A. S. Rupyshv, E. V. Semenov, V. S. Kulikauskas, and V. V. Zatekin, “Study of tungsten as a plasma-facing material for a fusion reactor,” *Phys. Procedia* **71**, 63–67 (2015).
- ⁸N. R. Schwartz, J. R. Nicholas, Z. J. Jackson, and P. T. Ireland, “Development of a novel DEMO divertor target: Spiral plate module,” *Phys. Scr.* **96**(12), 124027 (2021).
- ⁹G. Janeschitz, “Plasma-wall interaction issues in ITER,” *J. Nucl. Mater.* **290–293**, 1–11 (2001).
- ¹⁰H. Bolt, V. Barabash, G. Federici, J. Linke, A. Loarte, J. Roth, and K. Sato, “Plasma facing and high heat flux materials—Needs for ITER and beyond,” *J. Nucl. Mater.* **307–311**, 43–52 (2002).
- ¹¹T. Loewenhoff, A. Bürger, J. Linke, G. Pintsuk, A. Schmidt, L. Singheiser, and C. Thomser, “Evolution of tungsten degradation under combined high cycle edge-localized mode and steady-state heat loads,” *Phys. Scr.* **2011**, 014057 (2011).
- ¹²X. Hu, T. Koyanagi, M. Fukuda, N. A. P. K. Kumar, L. L. Snead, B. D. Wirth, and Y. Katoh, “Irradiation hardening of pure tungsten exposed to neutron irradiation,” *J. Nucl. Mater.* **480**, 235–243 (2016).
- ¹³J. Reiser, L. Garrison, H. Greuner, J. Hoffmann, T. Weingärtner, U. Jäntschi, M. Klimenkov, P. Franke, S. Bonk, C. Bonnekoh, S. Sickinger, S. Baumgärtner, D. Bolich, M. Hoffmann, R. Ziegler, J. Konrad, J. Hohe, A. Hoffmann, T. Mrotzek, M. Seiss, M. Rieth, and A. Möslang, “Ductilisation of tungsten (W): Tungsten laminated composites,” *Int. J. Refract. Met. Hard Mater.* **69**, 66–109 (2017).
- ¹⁴T. Smid, M. Akiba, G. Vieider, and L. Plöchl, “Development of tungsten armor and bonding to copper for plasma-interactive components,” *J. Nucl. Mater.* **258–263**, 160–172 (1998).
- ¹⁵R. A. Murgatroyd and B. T. Kelly, “Technology and assessment of neutron absorbing materials,” *At. Energy Rev.* **15**(1), 3–74 (1977).
- ¹⁶J. P. B. William, M. Mueller, and G. G. Libowitz, *Metal Hydrides* (Academic Press Inc., 1968), p. 119.

- ¹⁷T. Iwasaki and K. Konashi, "Development of hydride absorber for fast reactor—Application of hafnium hydride to control rod of large fast reactor," *J. Nucl. Sci. Technol.* **46**(8), 874–882 (2009).
- ¹⁸T. Hayashi, K. Tobita, S. Nishio, K. Ikeda, Y. Nakamori, and S. Orimo, "Neutronics assessment of advanced shield materials using metal hydride and borohydride for fusion reactors," *Fusion Eng. Des.* **81**(8–14), 1285–1290 (2006).
- ¹⁹M. N. Cinbiz, C. N. Taylor, E. Luther, H. Trelue, and J. Jackson, "Considerations for hydride moderator readiness in microreactors," *Nucl. Technol.* **209**, S136–S145 (2022).
- ²⁰C. Ang, L. Snead, and J. R. Trelewicz, "An innovative approach to composite moderators containing zirconium hydrides," *Transactions* **121**(1), 683–685 (2019).
- ²¹K. Kiuchi and R. B. McLellan, "The solubility and diffusivity of hydrogen in well-annealed and deformed iron," *Acta Metall. Mater.* **31**(7), 961–984 (1983).
- ²²R. B. McLellan and P. L. Sutter, "Thermodynamics of the hydrogen-nickel system," *Acta Metall.* **32**(12), 2233–2239 (1984).
- ²³V. Nemanič, "Hydrogen permeation barriers: Basic requirements, materials selection, deposition methods, and quality evaluation," *Nucl. Mater. Energy* **19**, 451–457 (2019).
- ²⁴L. L. Snead, N. Brown, J. R. Trelewicz, C. Ang, B. Cheng, X. Hu, and D. J. Sprouster, "Fabrication of two-phase composite moderators as potential lifetime reactor components," *Transactions* **121**(1), 1445–1447 (2019).
- ²⁵B. Cheng, E. M. Duchnowski, D. J. Sprouster, L. L. Snead, N. R. Brown, and J. R. Trelewicz, "Ceramic composite moderators as replacements for graphite in high temperature microreactors," *J. Nucl. Mater.* **563**, 153591 (2022).
- ²⁶L. L. Snead, D. Sprouster, B. Cheng, N. Brown, C. Ang, E. M. Duchnowski, X. Hu, and J. Trelewicz, "Development and potential of composite moderators for elevated temperature nuclear applications," *J. Asian Ceram. Soc.* **10**(1), 9–32 (2022).
- ²⁷D. Bhardwaj, B. Cheng, D. J. Sprouster, W. S. Cunningham, N. Rani, J. R. Trelewicz, and L. L. Snead, "Fabrication of neutron absorbing metal hydride entrained ceramic matrix shield composites," *Front. Nucl. Eng.* **3**, 1352667 (2024).
- ²⁸M. H. Mintz, "Hafnium-hydrogen," *Solid State Phenom.* **49–50**, 331–356 (1996).
- ²⁹S. S. Sidhu, L. Heaton, and D. D. Zaubers, "Neutron diffraction studies of hafnium-hydrogen and titanium-hydrogen systems," *Acta Crystallogr.* **9**, 607–614 (1956).
- ³⁰S. S. Sidhu and J. C. McGuire, "An x-ray diffraction study of the hafnium-hydrogen system," *J. Appl. Phys.* **23**(11), 1257–1261 (1952).
- ³¹M. Dottor, J.-C. Crivello, L. Laversenne, and J.-M. Joubert, "Experimental determination of the H-Hf phase diagram using *in situ* neutron diffraction," *J. Alloys Compd.* **937**, 168353 (2023).
- ³²L. J. Bannenberg, H. Schreuders, H. Kim, K. Sakaki, S. Hayashi, K. Ikeda, T. Otomo, K. Asano, and B. Dam, "Suppression of the phase coexistence of the fcc-fct transition in hafnium-hydride thin films," *J. Phys. Chem. Lett.* **12**(45), 10969–10974 (2021).
- ³³D. Coster, "On the x-ray spectra of hafnium and thulium," *London Edinburgh Dublin Philos. Mag. J. Sci.* **46**(275), 956–963 (1923).
- ³⁴R. V. Azhazha, K. V. Kovtun, S. V. Malykhin, B. A. Merisov, A. T. Pugachev, E. N. Reshetnyak, and G. Y. Kahadzhai, "Accumulation of hydrogen in hafnium: Structure and electrical resistivity," *Phys. Met. Metallogr.* **105**, 188–192 (2008).
- ³⁵H. Wang and K. Konashi, "Investigation on electronic, mechanical and thermal properties of Hf-H system," *J. Nucl. Mater.* **443**(1–3), 99–106 (2013).
- ³⁶M. Ito, K. Kurosaki, H. Muta, M. Uno, K. Konashi, and S. Yamanaka, "Thermal conductivity of hafnium hydride," *J. Nucl. Sci. Technol.* **46**(8), 814–818 (2009).
- ³⁷M. Ito, K. Kurosaki, H. Muta, M. Uno, K. Konashi, and S. Yamanaka, "Thermomechanical properties of hafnium hydride," *J. Nucl. Sci. Technol.* **47**(2), 156–159 (2010).
- ³⁸Y. Liu, X. Huang, D. Duan, F. Tian, H. Liu, D. Li, Z. Zhao, X. Sha, H. Yu, H. Zhang, B. Liu, and T. Cui, "First-principles study on the structural and electronic properties of metallic HfH₂ under pressure," *Sci. Rep.* **5**, 11381 (2015).
- ³⁹R. Quijano, R. de Coss, and D. J. Singh, "Electronic structure and energetics of the tetragonal distortion for TiH₂, ZrH₂, and HfH₂: A first-principles study," *Phys. Rev. B* **80**(18), 184103 (2009).
- ⁴⁰J. H. Weaver, D. J. Peterman, D. T. Peterson, and A. Franciosi, "Electronic structure of metal hydrides. IV. Ti H_x, Zr H_x, Hf H_x, and the fcc-fct lattice distortion," *Phys. Rev. B* **23**(4), 1692–1698 (1981).
- ⁴¹M. Kireš, "Archimedes' principle in action," *Phys. Educ.* **42**(5), 484 (2007).
- ⁴²H. M. Rietveld, "A profile refinement method for nuclear and magnetic structures," *J. Appl. Crystallogr.* **2**, 65–71 (1969).
- ⁴³R. Ruh and P. W. R. Corfield, "Crystal structure of monoclinic hafnia and comparison with monoclinic zirconia," *J. Am. Ceram. Soc.* **53**(3), 126–129 (1970).
- ⁴⁴A. Jain, S. P. Ong, G. Hautier, W. Chen, W. D. Richards, S. Dacek, S. Cholia, D. Gunter, D. Skinner, G. Ceder, and K. A. Persson, "Commentary: The materials genome approach to accelerating materials innovation," *APL Mater.* **1**(1), 011002 (2013).
- ⁴⁵B. Cekić, B. Prelesnik, S. Koićki, D. Rodić, M. Manasijević, and N. Ivanović, "Refinement of the crystal structure of Hf₂Fe," *J. Less-Common Met.* **171**(1), 9–15 (1991).
- ⁴⁶C. A. Schneider, W. S. Rasband, and K. W. Eliceiri, "NIH image to ImageJ: 25 years of image analysis," *Nat. Methods* **9**(7), 671–675 (2012).
- ⁴⁷I. Arganda-Carreras, V. Kaynig, C. Rueden, K. W. Eliceiri, J. Schindelin, A. Cardona, and H. Sebastian Seung, "Trainable Weka Segmentation: A machine learning tool for microscopy pixel classification," *Bioinformatics* **33**(15), 2424–2426 (2017).
- ⁴⁸H. Yan, N. Bouet, J. Zhou, X. Huang, E. Nazaretski, W. Xu, A. P. Cocco, W. K. S. Chiu, K. S. Brinkman, and Y. S. Chu, "Multimodal hard x-ray imaging with resolution approaching 10 nm for studies in material science," *Nano Futures* **2**(1), 011001 (2018).
- ⁴⁹A. Pattammattel, R. Tappero, M. Ge, Y. S. Chu, X. Huang, Y. Gao, and H. Yan, "High-sensitivity nanoscale chemical imaging with hard x-ray nano-XANES," *Sci. Adv.* **6**(37), eabb3615 (2020).
- ⁵⁰D. J. Sprouster, W. Streit Cunningham, G. P. Halada, H. Yan, A. Pattammattel, X. Huang, D. Olds, M. Tilton, Y. S. Chu, E. Dooryhee, G. P. Manogharan, and J. R. Trelewicz, "Dislocation microstructure and its influence on corrosion behavior in laser additively manufactured 316L stainless steel," *Addit. Manuf.* **47**, 102263 (2021).
- ⁵¹L. Li, H. Yan, W. Xu, D. Yu, A. Heroux, W.-K. Lee, S. Campbell, and Y. Chu, "PyXRF: Python-based x-ray fluorescence analysis package," *Proc. SPIE* **10389**, 103890U (2017).
- ⁵²A. Pattammattel, R. Tappero, Y. S. Chu, M. Ge, D. Gavrilov, X. Huang, and H. Yan, "Hard x-ray nano-XANES and implementation deep learning tools for multi-modal chemical imaging," *Proc. SPIE* **11839**, 118390J (2021).
- ⁵³K. Jorissen and J. J. Rehr, "New developments in FEF: FEF9 and JFEFF," *J. Phys.: Conf. Ser.* **430**, 012001 (2013).
- ⁵⁴M. Bauer, S. Müller, G. Kickelbick, and H. Bertagnolli, "The structures of the precursor Hf(OnBu)₄ and its modification in solution: EXAFS-investigation in combination with XANES- and IR-spectroscopy," *New J. Chem.* **31**(11), 1950 (2007).
- ⁵⁵M. S. Mathur, *The Engineering and Optimization of the Hafnium Based Metal Oxide Semiconductor Structure* (Chemical Engineering, University of California, Los Angeles, 2008).
- ⁵⁶D.-Y. Cho, T. J. Park, K. D. Na, J. H. Kim, and C. S. Hwang, "Structural disorders in an amorphous HfO₂ film probed by x-ray absorption fine structure analysis," *Phys. Rev. B* **78**(13), 132102 (2008).
- ⁵⁷D.-Y. Cho, H.-S. Jung, and C. S. Hwang, "Structural properties and electronic structure of HfO₂-ZrO₂ composite films," *Phys. Rev. B* **82**(9), 094104 (2010).
- ⁵⁸Y. Uehara, K. Kawase, J. i. Tsuchimoto, and T. Shibano, "X-ray absorption and emission spectroscopy at the Hf L1 edge of hafnium-(silicon)-oxide ultra-thin films," *J. Electron Spectrosc. Relat. Phenom.* **148**(2), 75–79 (2005).
- ⁵⁹J. Morais, L. Miotti, K. P. Bastos, S. R. Teixeira, I. J. R. Baumvol, A. L. P. Rotondaro, J. J. Chambers, M. R. Visokay, L. Colombo, and M. C. M. Alves, "Environment of hafnium and silicon in Hf-based dielectric films: An atomistic study by x-ray absorption spectroscopy and x-ray diffraction," *Appl. Phys. Lett.* **86**(21), 212906 (2005).

- ⁶⁰H. Wen, Y. Zhao, Z. Zhang, O. Ertorer, S. Dong, and E. J. Lavernia, "The influence of oxygen and nitrogen contamination on the densification behavior of cryomilled copper powders during spark plasma sintering," *J. Mater. Sci.* **46**(9), 3006–3012 (2011).
- ⁶¹Y. Arita, T. Ogawa, B. Tsuchiya, and T. Matsui, "Heat capacity measurement and DSC study of hafnium hydrides," *J. Therm. Anal. Calorim.* **92**(2), 403–406 (2008).
- ⁶²S. K. Dolukhanyan, A. G. Aleksanian, and A. G. Hakobian, "Interaction of hafnium with hydrogen and nitrogen in the combustion regime," *Int. J. Hydrogen Energy* **20**(5), 397–395 (1995).
- ⁶³W. M. Keely, "Differential thermal analysis study of the reduction of cobalt oxide, iron oxide, and copper oxide," *J. Chem. Eng. Data* **10**(2), 186–188 (1965).
- ⁶⁴A. V. Anupama, W. Keune, and B. Sahoo, "Thermally induced phase transformation in multi-phase iron oxide nanoparticles on vacuum annealing," *J. Magn. Mater.* **439**, 156–166 (2017).
- ⁶⁵Z. H. Zhang, F. C. Wang, S. K. Lee, Y. Liu, J. W. Cheng, and Y. Liang, "Microstructure characteristic, mechanical properties and sintering mechanism of nanocrystalline copper obtained by SPS process," *Mater. Sci. Eng. A* **523**(1–2), 134–138 (2009).
- ⁶⁶Z.-H. Zhang, F.-C. Wang, L. Wang, and S.-K. Li, "Ultrafine-grained copper prepared by spark plasma sintering process," *Mater. Sci. Eng. A* **476**(1–2), 201–205 (2008).
- ⁶⁷Z. Zhaohui, W. Fuchi, W. Lin, L. Shukui, and S. Osamu, "Sintering mechanism of large-scale ultrafine-grained copper prepared by SPS method," *Mater. Lett.* **62**(24), 3987–3990 (2008).
- ⁶⁸G. E. Lloyd, "Atomic number and crystallographic contrast images with SEM: A review of backscattered electron techniques," *Mineral. Mag.* **51**(359), 3–19 (1987).
- ⁶⁹M. Rowles, "The effect of data quality and model parameters on the quantitative phase analysis of x-ray diffraction data by the Rietveld method," *J. Appl. Crystallogr.* **54**(3), 878–894 (2021).
- ⁷⁰R. K. Edwards and E. Veleckis, "Thermodynamic properties and phase relations in the system hydrogen-hafnium," *J. Phys. Chem.* **66**(9), 1657–1661 (1962).
- ⁷¹C. Boelsma, L. J. Bannenberg, M. J. van Setten, N. J. Steinke, A. A. van Well, and B. Dam, "Hafnium—An optical hydrogen sensor spanning six orders in pressure," *Nat. Commun.* **8**, 15718 (2017).
- ⁷²G. Chen, K. D. Liss, G. Auchterlonie, H. Tang, and P. Cao, "Dehydrogenation and sintering of TiH₂: An *in situ* study," *Metall. Mater. Trans. A* **48**(6), 2949–2959 (2017).
- ⁷³S. Yamanaka, H. Ogawa, and M. Miyake, "Effect of interstitial oxygen on hydrogen solubility in titanium, zirconium, and hafnium," *J. Less Common Met.* **172–174**, 85–94 (1991).
- ⁷⁴H. Okamoto, M. E. Schlesinger, and E. M. Mueller, *Thermodynamics and Phase Diagrams* (ASM Handbook: Alloy Phase Diagrams, 2016).
- ⁷⁵L. Botti, S. A. Kondrat, R. Navar, D. Padovan, J. S. Martinez-Espin, S. Meier, and C. Hammond, "Solvent-activated hafnium-containing zeolites enable selective and continuous glucose-fructose isomerisation," *Angew. Chem. Int. Ed.* **59**(45), 20017–20023 (2020).
- ⁷⁶F. Predel, *Phase Equilibria, Crystallographic and Thermodynamic Data of Binary Alloys* (Springer-Verlag, Berlin, 2016).